mmSkin: An Over-gauze Wound Assessment System using Radio Frequency Technologies

Xiaoyu Zhang, Zhengxiong Li, Yanda Cheng, Chenhan Xu, Chuqin Huang, Emma Zhang, Ye Zhan, Wei Bo, Jun Xia, Wenyao Xu

Abstract—**Skin wounds are often covered with gauze to protect the injury and support the healing process. Accurate wound assessment is essential for monitoring healing progress and guiding treatment decisions. However, existing assessment methods typically require direct exposure of the wound, necessitating the removal of gauze when present. This process disrupts the healing environment and increases the risk of secondary infections. In this paper, we introduce mmSkin, an innovative over-gauze wound assessment system that utilizes millimeter-wave (mmWave) radar technology to evaluate wound characteristics without the need to remove the gauze. Central to this system is the principle that variations in skin moisture, a critical indicator of wound health, significantly influence mmWave signal strength. By analyzing these variations, mmSkin accurately identifies skin moisture levels, thereby enabling precise assessment of wound conditions. To achieve reliable sensing, mmSkin incorporates a denoised mmWave imaging algorithm designed to reduce motion noise and effectively distinguish between signals reflected from the target skin and those from surrounding environmental interference. Additionally, the system integrates a physics-based model to guide the training of its moisture derivation model. This integration ensures that mmSkin can accurately estimate moisture distribution across the wound area, making it a powerful tool for non-invasive wound assessment. Extensive experiments validate the system's high accuracy in over-gauze wound moisture distribution estimation, achieving a mean moisture error of approximately 0.5% in both wound phantom and invivo tests. Additionally, the system demonstrates a structural similarity index measure (SSIM) of about 0.9 compared to groundtruth moisture distributions in both test scenarios. These results highlight mmSkin's potential to revolutionize non-invasive wound assessment and improve patient outcomes.**

Index Terms—**mmWave sensor, over-gauze, wound assessment**

I. INTRODUCTION

Wound care is of paramount importance, as wounds affect millions of individuals, with over 8 million cases annually in the United States alone [1]. Chronic wounds, such as those associated with diabetic foot ulcers or peripheral vascular disease, and

Xiaoyu Zhang, Wei Bo and Wenyao Xu are with the Department of Computer Science and Engineering, State University of New York at Buffalo, Amherst, NY 14068 USA (email: zhang376@buffalo.edu, weibo@buffalo.edu, wenyaoxu@buffalo.edu).

Zhengxiong Li is with the Department of Computer Science and Engineering, University of Colorado Denver, Denver, CO 80204 USA (email: zhengxiong.li@ucdenver.edu).

Yanda Cheng, Chuqin Huang, Emma Zhang and Jun Xia are with the Department of Biomedical Engineering, State University of New York at Buffalo, Amherst, NY 14068 USA (email: yandache@buffalo.edu, chuqinhu@buffalo.edu, emmzhang1@gmail.com and junxia@buffalo.edu).

Chenhan Xu is with the Department of Computer Science, North Carolina State University, Raleigh, NC 27695 USA (email: cxu34@ncsu.edu).

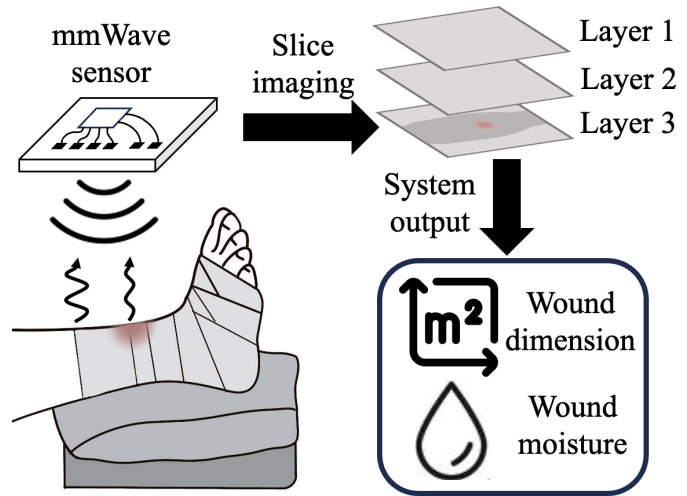Ye Zhan is with Linde Inc, Tonawanda, NY 14150 USA (email: ye.zhan@linde.com).

Fig. 1. The mmSkin system scans human wounds and provides a comprehensive assessment, including wound dimensions and moisture levels.

acute wounds from injuries or surgeries, represent significant challenges [2]. The economic burden is also substantial, with wound care costing over 22 billion per year in the U.S [3], [4]. This highlights the need for effective and innovative solutions to address both the clinical and financial aspects of wound management.

Current wound assessment practices predominantly depend on traditional in-hospital techniques, such as ruler-based measurements and more invasive methods like saline or gel injections [5], [6]. These approaches generally require the supervision of clinicians and are susceptible to inaccuracies due to the lack of objective and quantitative metrics [7], [8]. Additionally, invasive procedures can cause discomfort for patients and heighten the risk of secondary injuries [9]. These issues highlight the critical need for a non-invasive, reliable, and objective solution for assessing wounds.

The first generation of the method relies on non-invasive contact sensors, which require direct interaction with the wound. For example, researchers proposed the use of ultrasound devices to assess wound conditions [10]. However, this approach necessitates contacting wounds, increasing the risk of secondary infections and causing patient discomfort. The second generation introduces non-contact sensors. For instance, researchers developed techniques utilizing cameras to evaluate wound conditions without physical contact [11]. Despite this advancement, these sensors are unable to penetrate gauze, still requiring wound exposure during assessment. As a result, the

risk of infection remains when the wound is covered by gauze.

Building upon traditional methods, we introduce a third-generation technique: an RF-based over-gauze wound assessment method. Water serves as a critical biomarker for evaluating wound conditions, and due to its distinct response to RF signals, we utilize RF technology to assess wound status effectively. The penetrating capabilities of RF signals allow for the innovative assessment of wounds through gauze, thereby eliminating the necessity to remove the dressing [12]. This approach not only overcomes the limitations of previous methods but also improves patient comfort and safety while minimizing the risk of infection.

In this study, we develop a novel mmWave-based system for wound assessment, named mmSkin. In comparison to other RF-based techniques, the mmWave sensor offers several advantages [13], [14]. Firstly, it operates at high frequencies, providing millimeter-level resolution for more precise assessment. Secondly, its compact size allows easy integration into medical devices. Thirdly, it operates on low power, posing no threat to human health. Lastly, Commercial Off-The-Shelf (COTS) mmWave sensor is cost-effective, making it accessible for various scenarios.

In this paper, we explore the correlation between mmWave signals and water content in human wounds [15], as depicted in Figure 1. Our innovative mmSkin system leverages this relationship to enable multifaceted wound sensing applications. To mitigate environmental noise, we developed a denoised mmWave imaging algorithm that enhances signal clarity by strengthening the target signal and effectively separating it from background interference. The system's performance is validated through extensive experiments, achieving a mean moisture error of approximately 0.5% in both wound phantom and invivo tests. Furthermore, the system demonstrates a SSIM of about 0.9 when compared to groundtruth moisture distributions, highlighting its accuracy and reliability in wound moisture assessment.

The contributions are listed as follows:

- We develop mmSkin, the first over-gauze wound assessment system designed to minimize the risk of secondary infections by eliminating the need to remove gauze for wound evaluation.
- We develop a denoised mmWave imaging algorithm, which mitigates the impact of motion noise encountered during mmWave sensor movement in near-field wound scanning, thereby enhancing the wound assessment accuracy.
- Leveraging the intrinsic correlation between moisture and mmWave signals, we design a moisture derivation model that incorporates this physical relationship to guide and accelerate the training process for accurate moisture distribution estimation.
- We conduct extensive experiments to validate the system's performance in moisture distribution estimation across both wound phantom and invivo tests. Furthermore, we analyze both system-related and biological impact factors through comprehensive experiments, providing a thorough understanding of the system's capabilities and limitations.
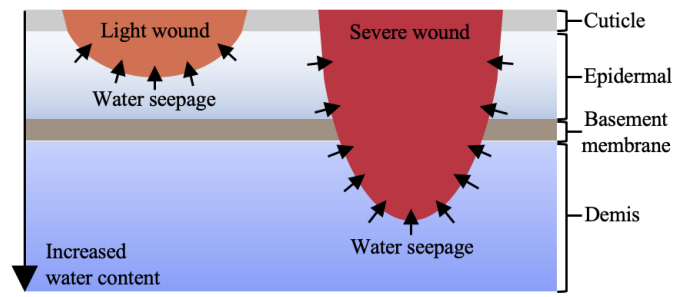

Fig. 2. Wound moisture levels increase due to water seepage from the skin, varying based on the severity of the wound.

II. BACKGROUND

A. Wound Assessment Biomarker: Moisture

Wounds can be categorized into acute types, such as those from injuries or surgeries, and chronic types, including diabetic foot ulcers and wounds related to peripheral vascular disease. Figure 2 illustrates the correlation between wound severity and moisture levels. Human skin is composed of multiple layers, including the cuticle, epidermis, basement membrane, and dermis. Under normal conditions, the cuticle and basement membrane function as protective barriers, preventing internal water content from seeping to the surface. However, wounds compromise these protective layers, leading to water seepage and causing wounds to appear moist. The extent of this moisture seepage depends on the severity of the wound. Light wounds typically damage only the upper layers of skin, resulting in minimal water loss. In contrast, severe wounds penetrate deeper into the dermis, where moisture levels are significantly higher. Consequently, severe wounds exhibit more pronounced moisture seepage, which is directly linked to higher external moisture levels. This variation in moisture serves as a vital biomarker for evaluating wound conditions and guiding treatment strategies.

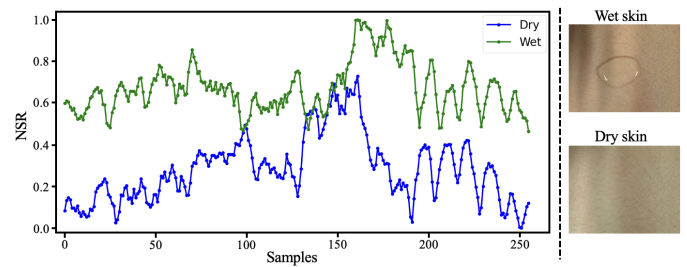### B. Fundamental of mmWave-based Moisture Sensing

Fig. 3. Normalized signal strength (NSR) of different mmWave data samples.

Current moisture sensing technologies are hindered by limitations such as their inability to penetrate gauze, necessitating direct exposure of wounds for accurate measurements. This requirement increases the risk of secondary infections and can lead to patient discomfort. mmWave-based moisture sensing utilizes the electromagnetic coupling effect, where water modifies the interaction between mmWave signals and

the skin, leading to variations in the strength of the reflected signal. As illustrated in Figure 3, we conduct an experiment on the forearms of a subject, altering the skin's moisture levels by wetting it and then analyzing the signal response. The findings reveal that higher moisture levels correspond to an increase in mmWave signal intensity, thereby establishing a direct correlation between moisture content and signal strength. These results highlight the potential of mmWave technology to accurately assess moisture levels, positioning it as a valuable tool for applications such as wound assessment.

C. Practical Challengers

To develop a practical mmWave-based wound assessment system, two key challenges must be addressed. First, environmental noise can degrade signal quality and compromise the accuracy of wound assessments. To mitigate this, a high-resolution mmWave imaging architecture is needed to effectively separate the wound signal from environmental noise. Second, a robust correlation model is required to extract multiple wound features from the mmWave signal—such as spatial distribution and dielectric properties—and accurately map these features to wound characteristics, including size and moisture.

III. mmSkin System Design

A. mmSkin Overview

The architecture of the mmSkin system is illustrated in Figure 4. Initially, the mmWave sensor conducts a two-dimensional (2D) scan of the wound area to capture raw mmWave data. This data undergoes processing through a denoising mmWave imaging algorithm, which incorporates Synthetic Aperture Radar (SAR) technology to enhance the spatial resolution of the images. The refined mmWave image is then analyzed by a moisture distribution derivation model, which extracts the moisture levels from the image. These moisture levels are critical for assessing the wound's condition. Subsequent sections of this document will delve deeper into the mmSkin framework, outlining its operational principles and the functionalities of its key components.

B. Radio Frequency Selection for Wound Assessment

When evaluating the capabilities of different frequency ranges for over-gauze wound assessment, a spectrum of capabilities emerges. Starting with microwave frequencies, which are situated below mmWave frequencies, they typically offer moderate resolution due to their longer wavelengths, particularly noticeable in the UHF and L-band regions. While they possess reasonable penetration abilities through fabric and certain materials, their capacity to precisely detect subtle changes in moisture is somewhat limited. In contrast, mmWave frequencies, which range from 30 GHz to 300 GHz, inherently provide high resolution because of their shorter wavelengths. This attribute enables them to effectively detect minor variations in skin moisture levels. Their penetration capabilities, while moderate, are adequate to traverse fabric occlusions, primarily focusing on the human skin surface. Beyond mmWave frequencies, sub-terahertz and terahertz ranges, with even

shorter wavelengths, offer exceptional resolution. However, a significant drawback is their penetration ability; these higher frequencies are more readily absorbed by materials and may not effectively penetrate fabric, which could limit their applicability in over-gauze wound scenarios. Overall, mmWave frequencies offer a balanced profile, making them an excellent choice for wound assessment under gauze occlusion conditions due to their combination of resolution and penetration capabilities.

C. Scanning Modality and Parameter Configuration

As shown in Figure 5, the commodity mmWave sensor transmits a Frequency-Modulated Continuous-Wave (FMCW) signal, and the frequency increases linearly over a cyclical period of time (i.e., chirp). f_s and B are the start frequency and bandwidth. The transmitted mmWave signal at the time t can be modeled as $f(t)$.

To enhance the spatial resolution in mmWave-based sensing, we have integrated the Synthetic Aperture Radar technique, enabling the mmWave sensor to navigate a 2D plane. This approach allows for the construction of an antenna aperture significantly larger than the actual size of the sensor's antenna. Illustrated in Figure 6, the mmWave sensor systematically moves across the 2D plane, uniformly sampling one chirp at each location. dx and dy are the step distance in X axis and Y axis. Additionally, the mmWave sensor collects T samples at each location. Therefore, the mmWave signal can be modeled as $f(x, y, t)$, where x and y represent the position of $x \cdot dx$ and $y \cdot dy$ in the X axis and Y axis, t represent the sample index in the T samples. Also, $x \in [1, \mathcal{X}]$ and $y \in [1, \mathcal{Y}]$, with $\mathcal{X}$ and $\mathcal{Y}$ denoting the number of scanning locations along the X and Y axes, respectively.

D. Denoised mmWave Imaging in Near-Field Wound Assessment

The mmWave signal collected at a location $f(x, y, t)$ is the overlay of reflected signals from different objects in the environment. In this section, we design a denoised mmWave imaging method to decipher this complex signal and get the target-related information. First, we apply a Fast Fourier Transform (FFT) along the sample dimension. This transforms the initial signal $f(x, y, t)$ into a range bin profile $R(x, y, k)$, a process known as Range-FFT. Variant $k \in K$ corresponds to the range index in the range bin profile. As outlined in Equation (1), by choosing the range index k calculated from the distance d of the mmWave sensor to the target, we enable the sensor to concentrate on the target. This selective focus ensures that the sensor primarily captures signals related to the target. In Equation (1), $Slope$ is the rate at which the frequency changes with respect to time, F_s is the sampling rate, c is the light speed, and T is the number of samples.

$$k = \frac{Slope}{F_s} \times \frac{2d}{c} \times T. \qquad (1)$$

The conventional mmWave imaging algorithm [16] operates under the assumption that the mmWave sensor maintains a consistent distance to the target across different scanning locations. This assumption holds when the target is far from
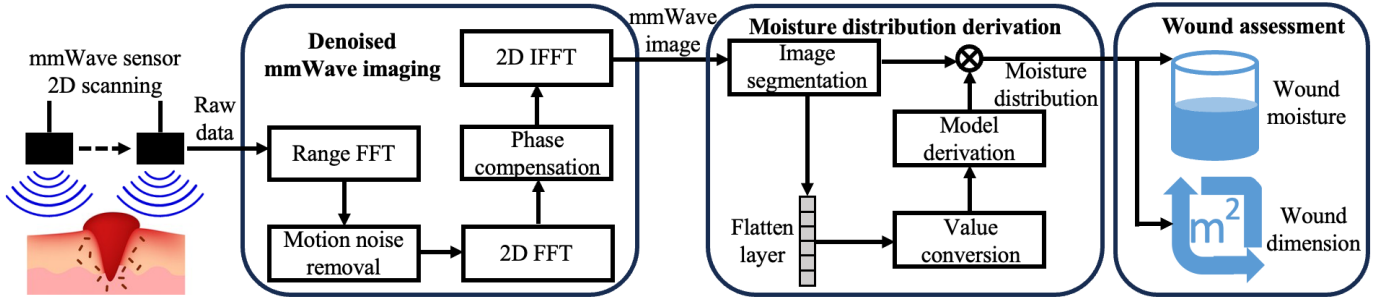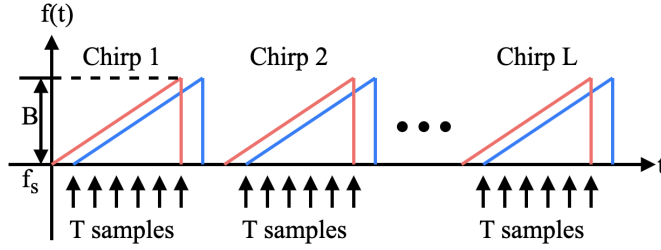
Fig. 4. Framework of the mmSkin system.

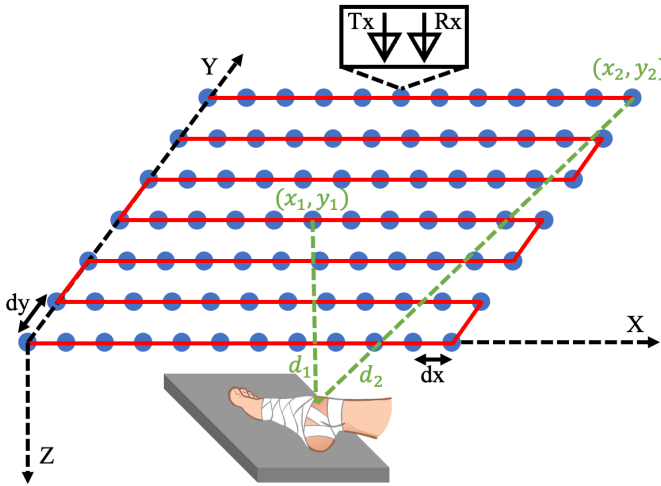Fig. 5. One frame structure of the mmWave sensor.

Fig. 6. Diagram illustrating the use of a mmWave sensor to scan a human wound for assessment.

Algorithm 1 Denoised mmWave imaging algorithm.

1: The mmWave sensor uniformly moves and collects the signal $f(x,y,t), x \in [1,\mathcal{X}], y \in [1,\mathcal{Y}], t \in [1,T]$ in the 2D plane.

2: Assume the mmWave scanning plane is in the X-Y plane, given the coordinate of the target center and each scanning location: (p_x, p_y, p_z) and $(x \cdot dx, y \cdot dy, 0)$.

3: Perform FFT on the third dimension T to get range bin profile $R(x,y,k)$.

4: **for** $x = 1, ..., \mathcal{X}$ **do**

5:     **for** $y = 1, ..., \mathcal{Y}$ **do**

6:         Calculate the distance from each mmWave location to the target $d = \sqrt{(x \cdot dx - p_x)^2 + (y \cdot dy - p_y)^2 + (p_z)^2}$.

7:         Calculate the range index k_{xy} based on Equation (1)

8:     **end for**

9: **end for**

10: Perform 2D FFT on $R(x,y)|_{k=k_{xy}}$, i.e., $FT_{2D}[R(x,y)|_{k=k_{xy}}]$.

11: Perform the phase compensation by multiplying $FT_{2D}[R(x,y)|_{k=k_{xy}}]$ with $e^{-j\sqrt{4\omega^2 - \omega_x^2 - \omega_y^2}p_z}$.

12: Perform 2D IFFT and calculate the amplitude to get the final 2D mmWave image $r(x,y), x \in [1,\mathcal{X}], y \in [1,\mathcal{Y}]$.

Next, the transformed mmWave signal $R(x,y)|_{k=k_{xy}}$ is used to reconstruct the mmWave image $r(x,y)$ based on Equation (2) [17].

$$r(x,y) = |FT_{2D}^{-1}[FT_{2D}[R(x,y)|_{k=k_{xy}}]e^{-j\sqrt{4\omega^2 - \omega_x^2 - \omega_y^2}p_z}]|, \quad (2)$$

while FT_{2D} and FT_{2D}^{-1} are 2D Fourier Transform and Fourier Inverse Transform. p_z represents the distance from the target to the mmWave scanning plane, x and y are indexed in X and Y axes. $r(x,y), x \in [1,\mathcal{X}], y \in [1,\mathcal{Y}]$ is the mmWave channel gain of the target at the location of $(x \cdot dx, y \cdot dy, p_z)$, ω_x and ω_y are the space frequencies of the 2D plane. The specific steps of the denoised mmWave imaging algorithm are detailed in Algorithm 1.

E. Moisture Distribution Derivation

Using our advanced denoising mmWave imaging algorithm, the 2D mmWave image is reconstructed to accurately depict both the target area and its surrounding environment. For the

the sensor, as the relative distance change due to location shifts becomes negligible. However, in human wound assessment, the proximity of the mmWave sensor to the target challenges this assumption. As depicted in Figure 6, the sensor at location (x_2, y_2) is further from the target compared to (x_1, y_1), meaning $d_1 < d_2$. Consequently, when conducting Range-FFT, the range indices for these locations might differ ($k_1 \neq k_2$). This discrepancy in range index selection can cause the mmWave sensor to erroneously focus on environmental noise rather than the target. Our denoised mmWave imaging algorithm addresses this by selecting the target based on the actual distance from each scanning location, ensuring consistent focus on the target. Therefore, we obtain a transformed mmWave signal represented as $R(x,y)|_{k=k_{xy}}, x \in [1,\mathcal{X}], y \in [1,\mathcal{Y}]$, which is highly related to the target.

task of deriving moisture distribution from mmWave signal response images, we use a Physics-informed neural network (PINN) model, which is particularly suited to addressing the challenge of data scarcity. The relationship between mmWave signal responses and skin moisture is dictated by physical laws pertaining to the interaction of electromagnetic waves with biological tissues. Collecting a substantial volume of high-quality labeled data for training purely data-driven models is often not feasible. PINNs offer a solution to this challenge by incorporating known physical constraints directly into the model architecture, enabling it to learn accurate mappings even when available labeled data is limited. As depicted in Figure 7, the PINN model includes segmentation and derivation components, with further details on each provided in the subsequent sections.
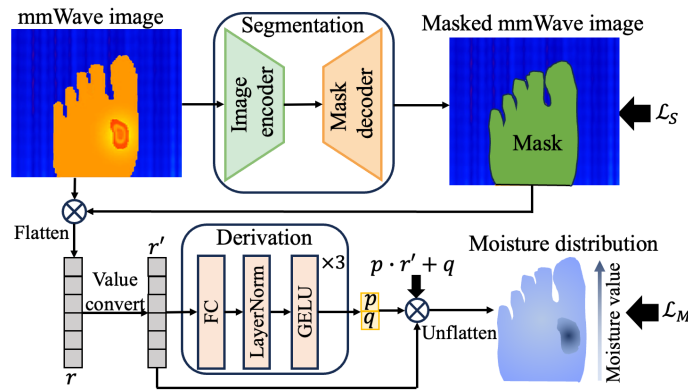

Fig. 7. The framework of the PINN model for evaluating moisture distribution.

1) mmWave Image Segmentation: To analyze the target, a segmentation model is required to separate the target from the denoised mmWave image. We use a segmentation model to segment the skin target based on the signal response difference between the skin target and the environment [18]. Specifically, when inputting a 2D image $r(x, y)$ to the segmentation model, a masked image $m(x, y), x \in [1, \mathcal{X}], y \in [1, \mathcal{Y}]$ with the same size as $r(x, y)$ will be obtained, while each pixel $m(x, y)$ has only two values: 0 or 1. If the pixel (x, y) is not marked as the target area, then the pixel value $m(x, y) = 0$, otherwise $m(x, y) = 1$. To restrict the performance of the model on the mmWave image segmentation, we introduce a loss function $\mathcal{L}_S$, which is represented as follows:

$$\mathcal{L}_S = \frac{1}{\mathcal{X} \times \mathcal{Y}} \sum_{x,y} \mathcal{L}_{\text{pixel}}^{x,y}, \tag{3}$$

while $\mathcal{L}_{\text{pixel}}$ is a weighted combination of $\mathcal{L}_{\text{CE}}$ [19] and $\mathcal{L}_{\text{Dice}}$ [20] for each pixel:

$$\mathcal{L}_{\text{pixel}} = \delta_1 \mathcal{L}_{\text{CE}} + \delta_2 \mathcal{L}_{\text{Dice}}. \tag{4}$$

2) Physics-informed Moisture Derivation: The mmWave channel gain r is mainly determined by the reflection coefficient β and transmission path loss α [21]. In mmWave-based human wound assessment, the sensor emits the mmWave signal to the human skin and receives the reflected signal, the signal is transmitted in the air media all the time, thus transmission path loss α depends on the relative permittivity of the air, which is

very small that can be neglected, i.e., $\alpha \approx 1$. Additionally, the refraction coefficient β is the metric that measures the ratio of the mmWave signal being reflected by the boundary of two materials. According to the Fresnel Equations, the reflection coefficient is defined as $\beta = \frac{n_2 - n_1}{n_2 + n_1}$, where the mmWave signal transmits from the first medium with the refractive index n_1 to the second medium with the refractive index n_2. In mmWave-based human wound assessment, the first medium is the air with a refractive index $n_1 \approx 1$, and the second medium is the human skin. The relationship between the mmWave signal channel gain r and the reflection coefficient β is described as follows:

$$r = c \cdot \alpha \cdot \beta = c \cdot \frac{n_{skin} - 1}{n_{skin} + 1}, \tag{5}$$

while c is a constant correlation coefficient and n_{skin} is the refractive index of the human skin. According to Equation (5), the mmWave signal channel gain r is only related to the refractive index of the human skin n_{skin}, which is the parameter that is the root of the relative dielectric constant ε [22], i.e., $n_{skin} = \sqrt{\varepsilon_{skin}}$.

In the field of skin moisture sensing, human skin is often conceptualized as a heterogeneous mixture primarily consisting of water and other biological components. The Looyenga formula [23] is a well-known model used to describe the dielectric properties of such mixtures, it models the correlation between the moisture level V and the relative dielectric constant of the human epidermal ε, which is described in Equation (6) as follows:

$$V = \frac{(\varepsilon^{\frac{1}{3}} - \varepsilon_{other}^{\frac{1}{3}})}{(\varepsilon_{water}^{\frac{1}{3}} - \varepsilon_{other}^{\frac{1}{3}})}, \tag{6}$$

The moisture level V is defined as the mass ratio of water to the target. The relative dielectric constants of water (ε_{water}) and other components (ε_{other}) within the target are intrinsic properties of these materials and are thus constants. Consequently, the moisture level V is determined by the relative dielectric constant of the human skin (ε). According to Equations (2&5&6), there exists a correlation between the mmWave image values and the moisture level, establishing a direct link between these two important parameters.

$$V = \frac{\left(\left(\frac{2c}{c-r} - 1 \right)^{\frac{2}{3}} - \varepsilon_{\text{other}}^{\frac{1}{3}} \right)}{\left(\varepsilon_{\text{water}}^{\frac{1}{3}} - \varepsilon_{\text{other}}^{\frac{1}{3}} \right)} = p \left(\frac{2c}{c-r} - 1 \right)^{\frac{2}{3}} + q = pr' + q,$$

$$p = \frac{1}{\left(\varepsilon_{\text{water}}^{\frac{1}{3}} - \varepsilon_{\text{other}}^{\frac{1}{3}} \right)}, q = -\frac{\varepsilon_{\text{other}}^{\frac{1}{3}}}{\left(\varepsilon_{\text{water}}^{\frac{1}{3}} - \varepsilon_{\text{other}}^{\frac{1}{3}} \right)}, r' = \left(\frac{2c}{c-r} - 1 \right)^{\frac{2}{3}}. \tag{7}$$

As shown in Figure 7, after obtaining the segmented mmWave image, a derivation module is employed to extract the p and q parameters, which are subsequently used to calculate the moisture distribution from the segmented mmWave image. Specifically, the loss function $\mathcal{L}_M$ is designed to guide the model in evaluating the moisture based on the physical relationship between the mmWave signal response and the moisture level:

$$\mathcal{L}_M = \frac{1}{\mathcal{X} \times \mathcal{Y}} \sum_{x,y} (V_G^{x,y} - p \times r'_{x,y} - q). \tag{8}$$

3) Total Loss Function of PINN model: The total loss function of our proposed PINN model is the combined loss function of the segmentation module and the derivation module, allowing the model to focus on the skin target area and accurately derive the moisture distribution. The combined loss function $\mathcal{L}$ is expressed as follows:

$$\mathcal{L} = \gamma_1 \mathcal{L}_S + \gamma_2 \mathcal{L}_M. \tag{9}$$

IV. IMPLEMENTATION AND EVALUATION

A. mmSkin System Integration

1) 2D scanning kit: In the setup illustrated in Figure 8, data collection is carried out using the mmWave sensor (TI AWR1642BOOST [24]). The sensor is attached to two linear motion guides arranged perpendicularly, forming a 2D motion platform (THOMSON LINEAR MOTION SYSTEM [25]), and moves at a constant speed across the 2D plane. During its motion, the sensor scans the target and generates the mmWave image using the imaging algorithm detailed in Section III-D. To ensure accurate data alignment, the controller (ELEGOO UNO R3 [26]) generates stable square waves as the trigger signal to simultaneously hardware trigger the mmWave sensor to start data sampling and the 2D motion platform to move the mmWave sensor in a 2D plane, allowing us to match the mmWave sensor's frame index with its corresponding location based on the known speed and frame sampling rate.
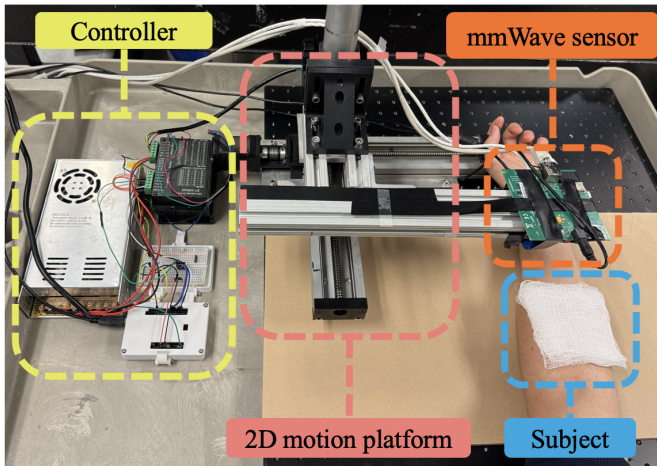

Fig. 8. mmSkin system prototype.

2) System Parameter Setup: The system parameters of our mmSkin system in the experiment are shown in Table I, the 2D motion platform moves the mmWave sensor at a uniform speed of 50 mm/s along both the X and Y axes. A single transmitter (Tx) and receiver (Rx) are used in the mmWave sensor for data acquisition. The FMCW frame period is set to 0.025 seconds, containing only one chirp. With a chirp duty cycle of about 0.3% of the total frame period, the short chirp duration ensures that the sensor remains effectively stationary during data collection at each position. The 2D scanning array consists of 51 positions along both the X and Y axes, denoted as $\mathcal{X} = 51$ and $\mathcal{Y} = 51$. The step size between each scanning point is 2 mm along both axes, resulting in a total scanning

length of $Dx = 100$ mm and $Dy = 100$ mm. The entire scan takes 102 seconds under these settings. The distance between the target and the scanning plane is set at 30 mm. During each chirp, the mmWave sensor operates with a frequency sweep ranging from 77 GHz to 81 GHz, providing the 4 GHz bandwidth. The frequency slope, B, is 46.493 MHz/μs, and the sensor samples uniformly 512 times throughout each chirp period.

TABLE I
THE PARAMETER SETTINGS OF THE MMSKIN SYSTEM IN THE EXPERIMENT.

System Parameters	Value
Scanning speed	50 mm/s
Step size (X&Y axes)	2 mm
Scanning length (X&Y axes)	100 mm
Scanning locations (X&Y axes)	51
Sensor-skin distance	0.03 m
Scanning time cost	102 seconds
Frame period	0.025 seconds
Tx-Rx pair	1
Start frequency	77 GHz
Bandwidth	4 GHz
One chirp samples	512
Frequency slope	46.493 MHz/μs

3) Training Parameter: Our PINN model, developed using PyTorch and executed on an NVIDIA L40S GPU, employs the Adam optimizer. This optimizer is especially effective for complex models that process noisy datasets, such as our mmWave data, which is subject to multipath effects from the environment [27]. We initiate training with a learning rate of 1e-3 to ensure robust early-phase convergence and incorporate a learning rate decay strategy that applies a multiplicative factor of 0.9 every 5 epochs [28]. This decay mechanism is important for fine-tuning model parameters throughout training, thus avoiding the common deep learning pitfall of overshooting minima. The loss function weights—$\delta_1, \delta_2, \gamma_1, \gamma_2$—set at 1, 1, 0.5, and 1 respectively, are meticulously configured to balance the dual objectives of fitting empirical data and adhering to the physical constraints that govern the underlying phenomena. Our training regimen spans 50 epochs with a batch size of 16, determined through empirical observation to optimize convergence trends. This approach ensures stable learning and prevents overfitting, allowing the model to achieve consistent and reliable performance without unnecessary complexity.

B. Evaluation Plan and Benchmark

1) Wound Phantom Fabrication: To evaluate the efficacy of the mmSkin system in wound assessment, we use a mixture of Agar powder [29] and water to mimic the human skin wound, which is easy to control and has the same material composition to the wound. As illustrated in Figure 9, we adjust the ratio of water to agar powder by mass, and pour the mixture into various molds of differing shapes and sizes. This approach enables the creation of wound phantoms with diverse geometries and moisture levels to represent the diverse nature of real wounds.

2) Invivo Test Benchmark: Due to the lack of access to real human wound samples, we simulate the abnormal moisture characteristics of wounds by applying ultrasound gel [30] to the skin. The more gel applied, the higher the simulated moisture
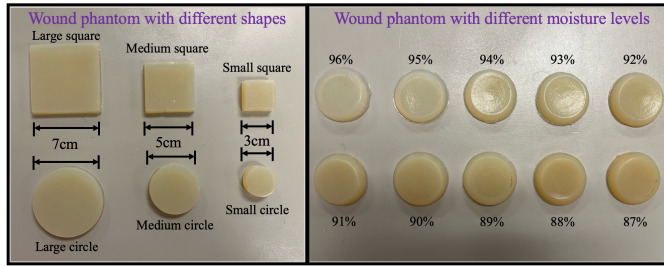
Fig. 9. Wound phantom with different shapes and moisture levels.

level, indicating a more severe wound condition. Compared to directly using water to mimic moisture variations, ultrasound gel is less prone to evaporation, allowing for a more stable simulation of wound conditions during the scanning process of the system.

C. Groundtruth Moisture Distribution

To obtain accurate ground truth data for moisture distribution, essential for training and testing our system, we utilize the capabilities of Short-wave Infrared (SWIR) light. SWIR light, covering wavelengths from 0.9 to 1.7 μm, has limited penetration capabilities but is significantly absorbed by water molecules. Therefore, areas of a wound with higher moisture levels will absorb more SWIR light, resulting in diminished reflected light intensity, which translates to lower pixel values in the SWIR camera images. As illustrated in Figure 10, we have developed a SWIR-based data collection platform and meticulously calibrated the SWIR camera to accurately measure moisture distribution [31]. The key components of the platform include:

(a) Light source: The light source [32] emits a broad spectrum, including SWIR light, onto the wound. The moisture in the wound absorbs a portion of the light energy, resulting in reflected light that encodes moisture information.

(b) Light source controller: The light source [33] manages the intensity of the emitted light from the light source, ensuring precise and consistent illumination for accurate data collection.

(c) Polarizer combination: Two polarizers [34] with aligned polarization directions are integrated into the platform. This setup improves the ratio of the surface reflection signal to the scattered signal originating from within the wound after passing through the second polarizer.

(d) SWIR camera: The WIDy SenS 640 SWIR camera [35] is employed to capture the reflected light and extract the moisture distribution of the wound.

D. Comparison between the mmSkin and SWIR systems

We simulate the skin wound following the method described in Section IV-B2 and conduct imaging using both the mmSkin system and the SWIR system. As shown in Figure 11, under the unobstructed condition, both systems clearly distinguish the skin area from the background and effectively identify the wound region on the skin. In the mmWave image, the wound area exhibits higher signal intensity due to the strong reflection of mmWave signals by water present in the wound. Conversely,
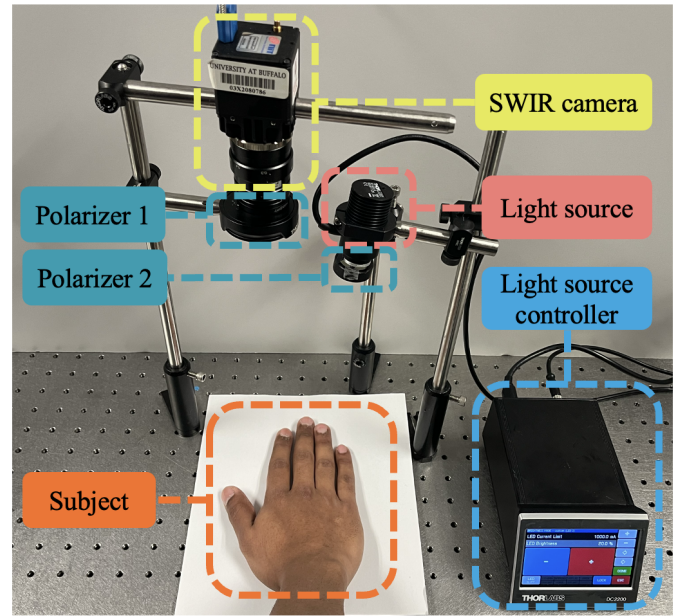

Fig. 10. SWIR-based moisture distribution measurement platform.

in the SWIR image, the wound area appears darker due to water's strong absorption of SWIR signals. However, when gauze is applied to cover the wound area, the SWIR system fails to display the wound condition due to its inability to penetrate the gauze. In contrast, the mmSkin system continues to provide effective imaging. This highlights the superiority of the mmSkin system for over-gauze wound assessment, enabling accurate evaluation of wounds covered by gauze without the risk of secondary infection caused by exposing the wound.
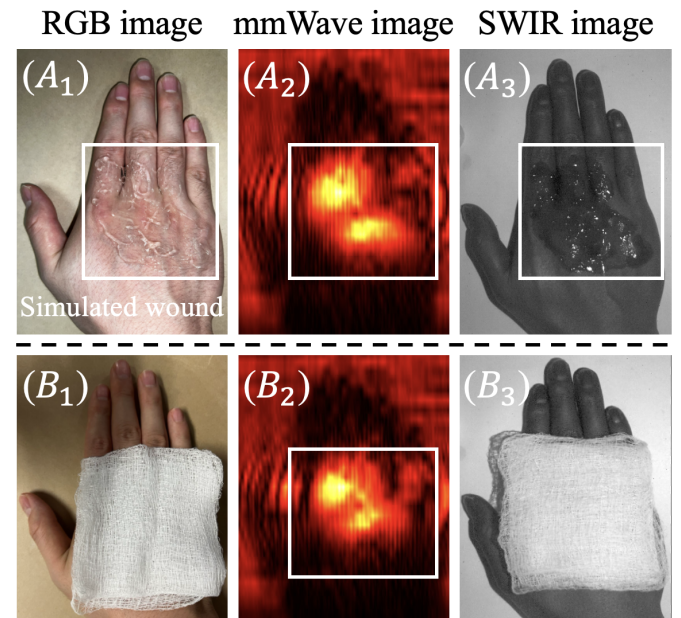

Fig. 11. Figure A_1, A_2 and A_3 show the RGB image, mmWave image, and SWIR image of the simulated wound on the human skin. Figure B_1, B_2 and B_3 display the corresponding images of the simulated wound covered with gauze.

E. Performance Metric

Mean Moisture Error (MME): The mean absolute error is used to quantify the moisture evaluation accuracy. For the output and groundtruth moisture distribution from the mmSkin and SWIR systems, the predicted value v and groundtruth value $\hat{v}$ are obtained by calculating the mean value of the moisture distribution. As described in Equation (10), MME is computed by taking the absolute differences between the two values, summing all n absolute differences, and then dividing by the number of predictions made. MME is a non-negative value, which indicates the accuracy of our mmSkin system in terms of moisture value estimation.

$$MME = \frac{1}{n} \sum_{i=1}^{n} |v_i - \hat{v}_i|. \tag{10}$$

Structural Similarity Index Measure (SSIM): The Structural Similarity Index [36] is a metric used to assess the similarity between two images. The SSIM formula is typically expressed as:

$$SSIM(x,y) = \frac{(2\mu_x\mu_y + C_1)(2\sigma_{xy} + C_2)}{(\mu_x^2 + \mu_y^2 + C_1)(\sigma_x^2 + \sigma_y^2 + C_2)}, \tag{11}$$

where μ_x and μ_y are mean values of image x and image y, σ_x^2 and σ_y^2 are the variances, σ_{xy} is the covariance between image x and image y, and C_1 and C_2 are regularization constants defined as $C_1 = (k_1 L)^2$ and $C_2 = (k_2 L)^2$. Here, L is the dynamic range of pixel values (i.e., $L = 255$ for 8-bit mmWave and SWIR images), while $k_1 = 0.01$ and $k_2 = 0.03$ are empirically determined scaling factors that align the metric with human visual sensitivity. These constants serve two purposes:
1. Numerical Stability: By adding C_1 and C_2 to the denominators, division-by-zero errors are avoided when the mean or variance terms $(\mu_x^2 + \mu_y^2)$ or $(\sigma_x^2 + \sigma_y^2)$ are extremely small (e.g., in uniform or near-uniform image regions).
2. Perceptual Relevance: The values of k_1 and k_2 are chosen to reflect the human visual system's tolerance to minor luminance and contrast variations (approximately 1% and 3% relative differences, respectively). For example, with $L = 255$, the resulting constants $C_1 = 6.5025$ and $C_2 = 58.5225$ ensure that SSIM prioritizes structural differences perceptible to humans while ignoring negligible fluctuations [37].
SSIM values range from -1 to 1, where 1 indicates perfect similarity, 0 means no similarity, and negative values suggest inverse correlation.

V. System Functional Study: Wound Phantom Test

As described in Section II-A, the wound condition is closely linked to the moisture level due to the water seepage effect. Therefore, wound assessment essentially involves evaluating the moisture distribution. In this section, we evaluate the impact of various factors on the moisture distribution assessment performance of the mmSkin system. To conduct an accurate analysis by controlling a single factor, we use the wound phantom introduced in Section IV-B1 as the test subject for its controllable shape and moisture. As illustrated in Figure 9, we create 60 distinct wound phantom subjects, each varying in shape or moisture level. In the following sections, we perform

a series of experiments using the created subjects for data collection.

A. System Factor Analysis

As outlined in Section III-D, the denoised mmWave imaging algorithm reduces motion noise during mmWave sensor scanning by synchronizing sensor-to-subject distance prior to imaging. To evaluate its effectiveness, we divide the 60 wound phantom subjects into 50 subjects for training and 10 subjects for testing. For each subject, we put it 3 cm directly below the center of the mmWave sensor scanning plane, rotate or flip the subject, and conduct 10 scans to collect 10 sets of data per subject. The dataset is trained and tested on two system pipelines:

1). **Comparison system:** Conventional mmWave imaging algorithm [16] combined with a PINN model.

2). **mmSkin system:** Denoised mmWave imaging algorithm combined with the same PINN model.

System performance is assessed on the testing dataset using the SSIM metric described in Section IV-E. Specifically, we compare the similarity between the system's output moisture distribution and the groundtruth moisture distribution obtained from the SWIR camera. As shown in Table II, the mmSkin system, utilizing the denoised mmWave imaging algorithm, outperform the comparison system in moisture distribution estimation. This improvement highlights the enhanced image quality provided by the denoised mmWave imaging algorithm, emphasizing its important role in the mmSkin system.

TABLE II
THE MEAN SSIM RESULTS FOR MOISTURE DISTRIBUTION ESTIMATION OF DIFFERENT SYSTEMS.

System Type	SSIM (Range from -1 to 1)
Comparison System	0.78
mmSkin System	**0.9**

B. Over-gauze Wound Assessment: Wound Phantom

Compared to existing wound assessment technologies, our system offers penetration capabilities, enabling wound evaluation without removing the gauze. This feature minimizes the risk of secondary infections. In this section, we assess the system's ability to perform over-gauze wound assessment, specifically focusing on moisture distribution estimation. As illustrated in Figure 12, we test the system using 10 wound phantom subjects from the testing dataset, each covered with gauze of varying thickness. For each subject, we collect 10 sets of data after randomly rotating and flipping the subject. The trained mmSkin system in Section V-A is then used to evaluate moisture distribution estimation across these 100 datasets. We compare the estimated moisture distribution with the groundtruth moisture distribution obtained from the SWIR camera, using the MME and mean SSIM value described in Section IV-E to quantify the accuracy. As shown in Figure 12, The experimental results conclusively demonstrate that the mmSkin system maintains consistent performance regardless of gauze

thickness (1–2 layers), achieving sub-1% MME (0.43–0.54%) and high SSIM values (0.88–0.91) across all tested occlusion conditions. Notably, the system's accuracy slightly improves with 2-layer gauze (MME=0.50%, SSIM=0.90) compared to 1-layer cases (MME=0.54%, SSIM=0.88), indicating that its robustness is not compromised by increased occlusion depth. The invariance to gauze thickness (1–2 layers) ensures reliable wound assessment in real-world scenarios where clinicians may apply varying numbers of dressing layers. With MME consistently below 0.55% and SSIM exceeding 0.88, the system minimizes false diagnoses—a vital requirement for efficient wound care.
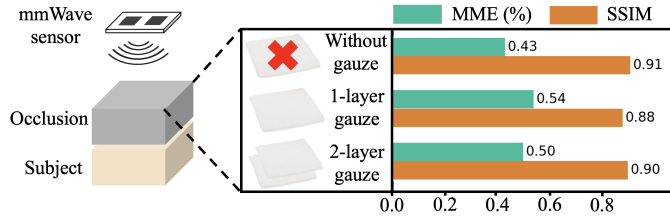

Fig. 12. The MME and mean SSIM results for moisture distribution estimation on the wound phantom under varying layers of gauze occlusion.

C. System Impact Factor

In this section, we evaluate the impact of four key system factors: the distance between the subject and the mmWave sensor, the angle of the subject relative to the mmWave sensor, the number of samples per scanning location, and the scanning speed. This analysis aims to provide a comprehensive understanding of the mmSkin system and identify the optimal parameter settings. The detailed evaluation process is discussed in the subsequent sections.

1) Sensor-subject Distance: In the mmSkin system, the mmWave sensor evaluates moisture by receiving signals reflected from the subject surface. However, when the distance between the subject and the mmWave sensor increases, the reflected signals from the subject are more susceptible to multipath interference caused by reflections from other objects in the environment. This interference can degrade the accuracy of moisture assessment. To evaluate the impact of the subject-to-sensor distance on the system's moisture distribution estimation performance, we conduct experiments by placing 60 subjects at varying distances from the center of the mmWave sensor scanning plane. For each subject, 10 sets of data are collected. The dataset from 50 subjects is used to train the system model, while the remaining dataset of 10 subjects is reserved for testing. We use the SSIM to evaluate the system performance under different distances. As shown in Figure 13, the system's moisture distribution estimation performance decreases as the distance increases, consistent with our expectations, demonstrating that shortening the subject to sensor distance is important for enhancing the wound assessment performance of the mmSkin system.

2) Sensor-subject Angle: In addition to sensor-subject distance, we also analyze the impact of sensor-subject angle on the system's performance. Specifically, as described in
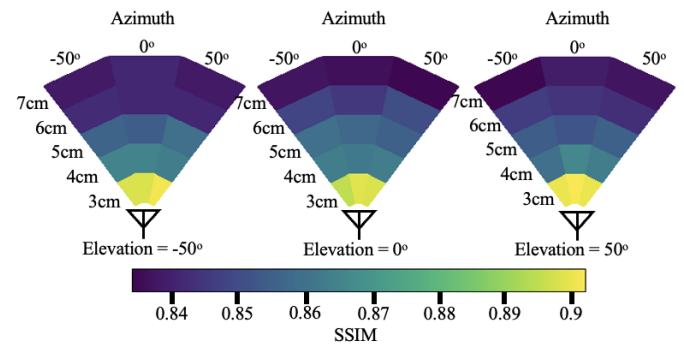

Fig. 13. The mean SSIM results for moisture distribution estimation under varying sensor-subject distance and sensor-subject angle.

Section V-C1, we place 50 subjects at a fixed distance below the mmWave scanning plane and collect data to train the mmSkin system under the sensor-subject angle of azimuth = $0°$, elevation = $0°$. Subsequently, we position another 10 subjects at various angles, including azimuth = $[-50°, 0°, 50°]$ and elevation = $[-50°, 0°, 50°]$, and perform multiple scans after rotation and flipping.

The data collected from these 10 subjects are used to test the trained mmSkin system's performance. As shown in the Figure 13, the system's performance remains consistent across different sensor-subject angles. This is because the system evaluates the moisture distribution of the subject, variations in angles only alter the subject's location within the mmWave image but do not affect the imaging accuracy, ensuring that the moisture estimation remains unaffected.

3) Number of Samples per Scanning Location: During the mmWave sensor scanning process for moisture analysis, data sampling is performed at each discrete, evenly spaced scanning location. We analyze the impact of the number of sampling points per data acquisition cycle in one scanning location on the system's moisture distribution evaluation performance. Specifically, we vary the sampling rates during data collection, resulting in different numbers of sampling points per acquisition cycle. Following the setup described in Section V-A, we use data from 50 subjects to train the mmSkin system and test the system's performance using an additional 10 subjects. The results, as shown in Figure 14, indicate that increasing the number of sampling points per scanning location improves the system's stability in moisture distribution evaluation. However, the overall accuracy remains unaffected. This is because a higher number of sampling points effectively reduces the influence of random noise but does not enhance the inherent quality of the received mmWave signals.

4) Scanning Speed: The mmWave sensor performs moisture evaluation by scanning the target, where faster scanning speeds result in shorter system latency but, theoretically, introduce greater motion noise. We conduct experiments to analyze the specific impact of scanning speed on system performance. Same as described in Section V-C3, the 60 subjects are split and scanned under five different scanning speeds: 30, 40, 50, 60, and 70 mm/s. We test the moisture distribution estimation performance of systems trained at corresponding scanning
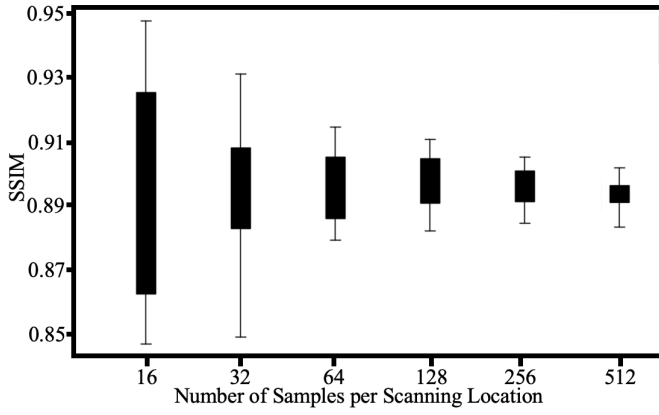
Fig. 14. The mean SSIM results for moisture distribution estimation under varying numbers of samples per scanning location.

speeds using the testing dataset. As shown in Figure 15(a), the system's performance significantly deteriorates when the scanning speed exceeds 50 mm/s. Figure 15(b) illustrates the underlying reason: higher scanning speeds introduce noticeable motion noise, which degrades image quality and subsequently affects the system's performance.
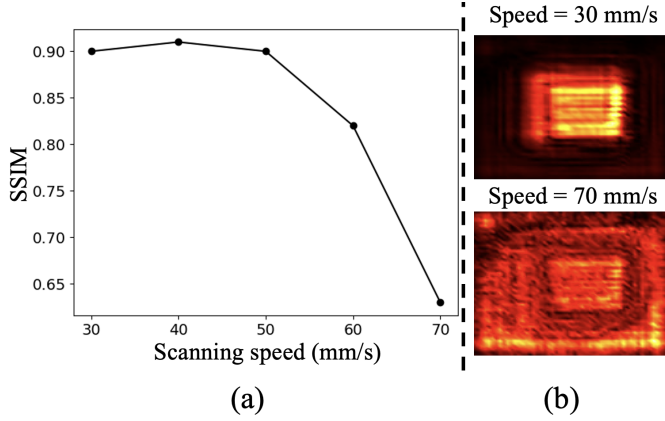

Fig. 15. (a) The mean SSIM results for moisture distribution estimation under varying scanning speed. (b) The comparison of mmWave images obtained at scanning speeds of 30 mm/s and 70 mm/s.

VI. SYSTEM PRACTICAL STUDY: INVIVO TEST

In this section, we investigate the performance of the mmSkin system in over-gauze wound assessment on real human skin and analyze the impact of various bio-impact factors on the system's performance. As described in Section IV-B2, due to the lack of real patient wound subjects, we simulate realistic wounds by applying ultrasound gel on the skin. A larger amount of ultrasound gel corresponds to higher moisture levels, representing more severe wound conditions. The following sections provide a detailed discussion of the invivo experimental setup and findings.

A. Over-gauze Wound Assessment: Invivo Test

First, we examine the performance of the mmSkin system in over-gauze wound assessment on real human skin, specifically

for moisture distribution estimation. In this study, we recruit 10 volunteers aged from 18 to 28, including 7 males and 3 females. Simulated wounds are created by applying ultrasound gel on various skin areas. For each participant, 50 data samples are collected. The training dataset is composed of data from 5 male and 2 female participants, while the remaining 2 male and 1 female participants are included in the testing dataset to evaluate the system's performance.

Furthermore, for the subjects in the testing dataset, we cover the simulated wounds with gauze of varying thicknesses, collect additional data, and evaluate the system's over-gauze performance. As shown in Table III, the system's moisture distribution estimation remain largely unaffected by the presence of gauze, demonstrating the system's capability to perform reliable wound assessment under over-gauze conditions.

TABLE III
THE MME AND MEAN SSIM RESULTS FOR MOISTURE DISTRIBUTION
ESTIMATION ON REAL SKIN UNDER DIFFERENT OVER-GAUZE CONDITIONS.

Gauze Thickness	MME	SSIM (Range from -1 to 1)
Without Gauze	0.54%	0.85
1-layer Gauze	0.5%	0.86
2-layer Gauze	0.57%	0.83

B. Bio-impact Factors

In this section, we investigate the effects of various bio-impact factors on the performance of the mmSkin system, i.e., skin tone, subject age and subject gender.

1) Skin tone: Skin tone is an important bio-impact factor, significantly affecting the performance of optical devices, such as cameras. To evaluate its influence on the mmSkin system's moisture distribution estimation, we utilize the dataset from 10 volunteers described in Section VI-A to train a mmSkin system. Additionally, we recruit three extra subjects representing three distinct skin tones based on the Fitzpatrick scale in the medical standard [38]. For each subject, 50 data samples are collected to test the mmSkin system's performance. As illustrated in Figure 16, skin tone has negligible impact on the mmSkin system's performance. This is because the mmWave signal exhibits strong robustness to variations in skin tone, making the system effective across a diverse range of skin colors.
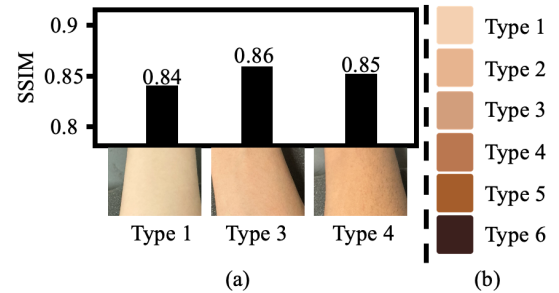

Fig. 16. (a) is the mean SSIM results for moisture distribution estimation under varying skin tones. (b) represents the Fitzpatrick scale, a medical standard used as a reference for skin tone classification.

2) Age: Age is another important bio-impact factor, as older individuals often have less elastic or drier skin [39], which might affect the system's moisture evaluation for wounds. To investigate this, we analyze the influence of age on system performance. First, we train a mmSkin system using the dataset of 10 volunteers described in Section VI-A. Next, we recruit three additional subjects aged 12, 40, and 45, none of whom fall within the age range of the training dataset of the mmSkin system. For each subject, 50 data samples are collected to test the mmSkin system. We compare the system's moisture distribution estimation with the groundtruth obtained from the SWIR camera, using SSIM as the evaluation metric. The system achieved SSIM scores of **0.84**, **0.82**, and **0.85** for the three subjects, respectively, indicating no significant impact on performance. The primary reason for this robustness is that age-related variations in skin moisture are minimal compared to the significant differences in moisture levels on wound surfaces. Thus, age does not substantially affect the system's ability to analyze wound moisture distribution.

3) Gender: As differences in skin moisture levels exist between males and females, we conduct experiments to evaluate the impact of gender-related moisture differences on the system's wound moisture assessment performance [40]. Specifically, using the dataset described in Section VI-A, we train the system model with the dataset from 7 male subjects and test the trained model on the dataset from 3 female subjects. The system's moisture distribution estimation accuracy is evaluated using SSIM, yielding a score of **0.86**. This result indicates that gender-related differences in skin moisture levels do not significantly affect the system's wound moisture assessment performance. We don't train the system model using the female subjects' dataset to test on the male subjects' dataset because the dataset, consisting of only three female subjects, is too limited to support effective system model training.

VII. DISCUSSION

A. mmSkin Scanning Speedup

By modifying the 2D motion stage type and substantially increasing its movement speed from 50 mm/s to 500 mm/s, the scanning duration can be notably reduced. The speed enhancement would have streamlined the process considerably. Moreover, the introduction of MMWCAS-RF-EVM board, equipped with an advanced 82 virtual antenna array, has augmented the scanning efficiency even further. By integrating these advancements, the scanning time can be further reduced to 10 seconds or less [41], [42]. Such improvements not only optimize the scanning process but can also greatly enhance user experience, operational throughput, and the overall efficacy of applications where time is an important factor.

B. Future Metrics

As the mmSkin system continues to develop and integrate into clinical settings, it becomes imperative to employ a comprehensive evaluation framework that encompasses a variety of performance metrics. These metrics, namely Signal-to-Noise Ratio (SNR), image resolution, system response time,

and cost, are critical for assessing the system's efficacy and viability in real-world applications.

SNR: The SNR is a fundamental metric for any imaging technology, where precision and clarity of the images are paramount [43]. High SNR values indicate a system's ability to distinguish signal from noise, which is crucial in clinical environments where background interference can affect image quality. Future evaluations will consider enhancing the SNR through advanced signal processing algorithms and hardware improvements, ensuring that the mmSkin system can deliver high-quality images even in challenging conditions [44], [45]. This enhancement will be vital for ensuring that the system can accurately detect subtle changes in wound conditions, a key factor in monitoring healing processes and detecting complications early.

Image Resolution: The mmSkin system's capability to image objects is a foundational achievement, but understanding the system's image resolution is paramount for real-world applications. Resolution can make a significant difference in the accuracy and clarity of the images produced, impacting the system's overall performance and applicability. By planning extensive experiments to evaluate the resolution, we can get a comprehensive understanding of the system's strengths and potential limitations. Furthermore, investigating the various factors that can influence the resolution will offer insights into optimizing the system for specific applications. By tailoring the system parameters based on these findings, the mmSkin system can be more effectively customized for different use cases, ensuring both efficiency and precision [46], [47], [48].

System Response Time: In emergency and clinical settings, the speed at which a system can process and display data is just as important as the accuracy of the data itself. The response time of the mmSkin system needs to be optimized to ensure that it can deliver real-time feedback to healthcare providers. Future iterations of the system will focus on minimizing processing time through more efficient data handling and faster computing hardware. This metric will be critical for the system's usability in fast-paced environments, ensuring that it can be seamlessly integrated into clinical workflows without causing delays [49], [50].

Cost: Cost-effectiveness remains a decisive factor in the widespread adoption of new medical technologies. The price of the mmSkin system must reflect its value to healthcare providers and patients, balancing affordability with advanced technology. Future evaluations will analyze the price in relation to the system's operational costs, potential savings from reduced complications or faster wound healing, and the benefits of non-invasive monitoring. Achieving a competitive price point while maintaining high quality and functionality will be key to the system's success in the market [51], [52].

C. Limitations and Future Work

Utilizing wound phantoms and simulating wounds on human skin provides an initial framework to evaluate the mmSkin system's capabilities. These models, being controlled and standardized, offer a consistent environment to gauge basic system performance. However, the complexities and variabilities inherent in real human wounds might present challenges

not encountered with the models. Particularly, the system's ability to penetrate various dressing materials, which may vary widely in composition and thickness [53], and its sensitivity to different wound components such as blood, pus, and necrotic tissues [21], [54], need thorough investigation. These elements can significantly alter the electromagnetic properties of the wound, affecting the mmWave signal's behavior. By planning to test the system on real human wounds in future studies, we aim to enhance its robustness and adaptability, ensuring it is equipped to handle the nuances of actual clinical scenarios. This approach not only preserves the initial study's intentions but also opens avenues for refining the technology based on direct clinical feedback and observations, ultimately increasing the system's clinical applicability and credibility.

VIII. RELATED WORK

Moisture Measurement: In the realm of moisture measurement, RF sensors are categorized based on their method of interaction with the target: contact and non-contact types. Contact RF moisture sensors engage directly with the target. These include Time-Domain Reflectometry (TDR) [55], [56], Frequency Domain Reflectometry (FDR) [57], [58], [59], and Capacitance sensors [60], [61]. TDR sensors, for instance, measure the time delay of a reflected signal to determine moisture levels, offering high accuracy but necessitating physical insertion into the target, which may be intrusive. FDR sensors evaluate changes in the frequency of an electromagnetic wave when it interacts with different moisture levels, providing the advantages of quick measurement cycles and ease of use, although they may offer less precision in targets with varied densities or compositions. Capacitance sensors work by detecting changes in capacitance due to variations in the dielectric constant of the target caused by moisture. These sensors are generally more affordable and adaptable to various targets but can be influenced by temperature fluctuations and often require calibration for specific applications.

Non-contact RF moisture sensors measure moisture without physical interaction with the material. This category includes microwave [62], [63], [64], radar-based systems [65], [66], [67], [68], [69] and Near-Infrared (NIR) reflectometry [70], [71], [72]. Microwave sensors operate on the principle of the dielectric constant, capitalizing on water's significant dielectric disparity with most materials, which enables deep penetration and robust performance in diverse environments, though they can be cumbersome and sensitive to material composition. NIR sensors, conversely, offer rapid surface moisture assessments through selective NIR light absorption by water molecules, susceptible to surface characteristics interference. Additionally, the poor penetration ability of the NIR light limits its availability in various applications. Radar-based systems offer non-invasive moisture detection through electromagnetic wave reflection analysis. Within this category, the mmWave sensor emerges as a superior choice, it possesses the unique capability to penetrate fabric without obstruction while refraining from deeply penetrating skin tissue, enabling precise focus on skin surface sensing. Moreover, the mmWave imaging algorithm proposed in this study, leveraging SAR technology, effectively enhances spatial resolution, thereby facilitating more precise skin surface moisture sensing.

mmWave Imaging Technologies: mmWave imaging capitalizes on the short wavelengths within the millimeter spectrum, facilitating high-resolution imaging suitable for diverse applications. Multiple Input Multiple Output (MIMO) [73], [74], [75] imaging leverages antenna arrays for both transmission and reception, creating detailed images that can differentiate between various targets and attributes concurrently. Meanwhile, beamforming [76], [46], [77], a sophisticated signal processing method employed in antenna arrays, concentrates the antenna's energy in targeted directions, thereby enhancing signal strength and spatial resolution. Contrasting with these methods, SAR [41], [78], [79], [80], [81] imaging constructs expansive, highly detailed images by moving a solitary antenna across a predetermined trajectory. Unlike MIMO and beamforming, whose imaging resolutions are tightly linked to the antenna array's dimensions, SAR circumvents this limitation, enabling high-resolution imaging without necessitating larger, more costly sensors. This is a pivotal reason our mmSkin system adopts SAR technology, aiming to deliver precision without increasing the system's size and cost.

IX. CONCLUSION

In our study, we introduce the mmSkin system, an emerging mmWave-based technology designed for over-gauze wound assessment. Our findings demonstrate mmSkin's capability to detect variations in water content through RF signal analysis and its potential in estimating wound moisture, which is closely linked to the wound's condition. The system integrates an innovative denoised mmWave imaging algorithm that effectively reduces motion noise, enhances spatial resolution, and distinguishes target signals from environmental interference. Furthermore, a moisture distribution derivation model is incorporated, leveraging the physical correlation between moisture and mmWave signal response to guide and expedite model training. The practicality of the mmSkin system has been validated through extensive testing, confirming its reliable performance on over-gauze wound assessment. This technology can significantly reduce the risk of infection by eliminating the need for gauze removal during assessment. In addition, as we explore its wide range of applications, the mmSkin system shows great promise as a valuable tool for non-invasive skin health monitoring, advancing the role of mmWave sensor technology in wound care.

REFERENCES

[1] Wound care. Available at: https://intermountainhealthcare.org/services/wound-care (accessed: 09.05.2024).

[2] Chronic wound affect. Available at: https://intermountainhealthcare.org/blogs/chronic-wounds-affect-65-million-in-us (accessed: 10.10.2024).

[3] Caroline E Fife and Marissa J Carter. Wound care outcomes and associated cost among patients treated in us outpatient wound centers: data from the us wound registry. *Wounds: a compendium of clinical research and practice*, 24(1):10–17, 2012.

[4] Koukab A Al-Gharibi, Sajana Sharstha, and Maria A Al-Faras. Cost-effectiveness of wound care: a concept analysis. *Sultan Qaboos University Medical Journal*, 18(4):e433, 2019.

[5] Sharon Baranoski and Elizabeth A Ayello. *Wound care essentials: Practice principles*. Lippincott Williams & Wilkins, 2008.

[6] II George Broughton, Jeffrey E Janis, and Christopher E Attinger. A brief history of wound care. *Plastic and reconstructive surgery*, 117(7S):6S–11S, 2006.

[7] Ruth Bryant and Denise Nix. *Acute and chronic wounds: current management concepts*. Elsevier Health Sciences, 2015.

[8] Health care. Available at: https://shcc.ufl.edu/services/primary-care/health-care-info-online/patient-education-wounds-caring-for/ (accessed: 05.12.2024).

[9] Cathy Thomas Hess. *Clinical guide to skin and wound care*. Lippincott Williams & Wilkins, 2012.

[10] Shuxin Li, Ali H Mohamedi, Jon Senkowsky, Ashwin Nair, and Liping Tang. Imaging in chronic wound diagnostics. *Advances in wound care*, 9(5):245–263, 2020.

[11] Lishuang Li, Yanan Sun, Honghui He, Gaiying He, Shuhua Ma, Weifeng Yang, and Yi Wang. Quantitative assessment of angiogenesis in skin wound healing by multi-optical imaging techniques. *Frontiers in Physics*, 10:894901, 2022.

[12] Yande Chen, Chongzhi Xu, Kexin Li, Jia Zhang, Xiuzhen Guo, Meng Jin, Xiaolong Zheng, and Yuan He. Wireless sensing for material identification: A survey. *IEEE Communications Surveys & Tutorials*, 2024.

[13] Anish Shastri, Neharika Valecha, Enver Bashirov, Harsh Tataria, Michael Lentmaier, Fredrik Tufvesson, Michele Rossi, and Paolo Casari. A review of millimeter wave device-based localization and device-free sensing technologies and applications. *IEEE Communications Surveys & Tutorials*, 24(3):1708–1749, 2022.

[14] Jia Zhang, Rui Xi, Yuan He, Yimiao Sun, Xiuzhen Guo, Weiguo Wang, Xin Na, Yunhao Liu, Zhenguo Shi, and Tao Gu. A survey of mmwave-based human sensing: Technology, platforms and applications. *IEEE Communications Surveys & Tutorials*, 2023.

[15] Zachary D Taylor, James Garritano, Shijun Sung, Neha Bajwa, David B Bennett, Bryan Nowroozi, Priyamvada Tewari, James W Sayre, Jean-Pierre Hubschman, Sophie X Deng, et al. Thz and mm-wave sensing of corneal tissue water content: in vivo sensing and imaging results. *IEEE transactions on terahertz science and technology*, 5(2):184–196, 2015.

[16] Muhammet Emin Yanik and Murat Torlak. Millimeter-wave near-field imaging with two-dimensional sar data. *Proc. SRC Techcon*, (P093929), 2018.

[17] David M Sheen, Douglas L McMakin, and Thomas E Hall. Three-dimensional millimeter-wave imaging for concealed weapon detection. *IEEE Transactions on microwave theory and techniques*, 49(9):1581–1592, 2001.

[18] Alexander Kirillov, Eric Mintun, Nikhila Ravi, Hanzi Mao, Chloe Rolland, Laura Gustafson, Tete Xiao, Spencer Whitehead, Alexander C. Berg, Wan-Yen Lo, Piotr Dollár, and Ross Girshick. Segment anything. *arXiv:2304.02643*, 2023.

[19] T-YLPG Ross and GKHP Dollár. Focal loss for dense object detection. In *proceedings of the IEEE conference on computer vision and pattern recognition*, pages 2980–2988, 2017.

[20] Fausto Milletari, Nassir Navab, S Ahmadi Ahmadi, and V Net. Fully convolutional neural networks for volumetric medical image segmentation. In *Proceedings of the 2016 Fourth International Conference on 3D Vision (3DV)*, pages 565–571.

[21] Chenshu Wu, Feng Zhang, Beibei Wang, and KJ Ray Liu. msense: Towards mobile material sensing with a single millimeter-wave radio. *Proceedings of the ACM on Interactive, Mobile, Wearable and Ubiquitous Technologies*, 4(3):1–20, 2020.

[22] David L Andrews. *Photonics, Volume 2: Nanophotonic Structures and Materials*. John Wiley & Sons, 2015.

[23] H Looyenga. Dielectric constants of heterogeneous mixtures. *Physica*, 31(3):401–406, 1965.

[24] Awr1642boost. Available at: https://www.ti.com/tool/AWR1642BOOST (accessed: 06.10.2024).

[25] Linear motion systems. Available at: https://www.thomsonlinear.com/en/products/linear-motion-systems (accessed: 01.10.2024).

[26] Uno r3 super starter kit. Available at: https://www.elegoo.com/products/elegoo-uno-r3-super-starter-kit (accessed: 10.09.2024).

[27] Zijun Zhang. Improved adam optimizer for deep neural networks. In *2018 IEEE/ACM 26th international symposium on quality of service (IWQoS)*, pages 1–2. Ieee, 2018.

[28] Kaichao You, Mingsheng Long, Jianmin Wang, and Michael I Jordan. How does learning rate decay help modern neural networks? *arXiv preprint arXiv:1908.01878*, 2019.

[29] Agar gel powder. Available at: https://www.amazon.com/NOW-Foods-Agar-Powder-5-Ounce/dp/B07DPVJ29T (accessed: 01.10.2023).

[30] Ultrasound gel. Available at: https://www.amazon.com/Aquasonic-Clear-Ultrasound-Squeeze-Bottle/dp/B08WQ2NRMV (accessed: 08.12.2023).

[31] Huining Li, Wenhan Zheng, Aditya Pandya, Chenhan Xu, Jun Xia, and Wenyao Xu. Smartphone-based blood perfusion assessment for ulcer care. In *Proceedings of the 20th ACM Conference on Embedded Networked Sensor Systems*, pages 843–844, 2022.

[32] Light source. Available at: https://www.thorlabs.com/thorproduct.cfm?partnumber=M1450L4 (accessed: 05.05.2024).

[33] Light source controller. Available at: https://www.thorlabs.com/thorproduct.cfm?partnumber=DC2200 (accessed: 03.10.2024).

[34] High contrast nir polarizing film. Available at: https://www.edmundoptics.com/p/high-contrast-nir-polarizing-film-25mm-x-25mm/50134/ (accessed: 03.07.2024).

[35] Swir. Available at: https://new-imaging-technologies.com/product/widy-sens-640/ (accessed: 05.15.2023).

[36] Umme Sara, Morium Akter, and Mohammad Shorif Uddin. Image quality assessment through fsim, ssim, mse and psnr—a comparative study. *Journal of Computer and Communications*, 7(3):8–18, 2019.

[37] Zhou Wang, Alan C Bovik, Hamid R Sheikh, and Eero P Simoncelli. Image quality assessment: from error visibility to structural similarity. *IEEE transactions on image processing*, 13(4):600–612, 2004.

[38] John D'Orazio, Stuart Jarrett, Alexandra Amaro-Ortiz, and Timothy Scott. Uv radiation and the skin. *International journal of molecular sciences*, 14(6):12222–12248, 2013.

[39] Hong Meng, Weixuan Lin, Yinmao Dong, Li Li, Fan Yi, Qingyang Meng, Yue Li, and Yifan He. Statistical analysis of age-related skin parameters. *Technology and Health Care*, 29(S1):65–76, 2021.

[40] Ethel Tur. Physiology of the skin—differences between women and men. *Clinics in dermatology*, 15(1):5–16, 1997.

[41] Muhammet Emin Yanik, Dan Wang, and Murat Torlak. Development and demonstration of mimo-sar mmwave imaging testbeds. *IEEE Access*, 8:126019–126038, 2020.

[42] Weiye Xu, Wenfan Song, Jianwei Liu, Yajie Liu, Xin Cui, Yuanqing Zheng, Jinsong Han, Xinhuai Wang, and Kui Ren. Mask does not matter: Anti-spoofing face authentication using mmwave without on-site registration. In *Proceedings of the 28th Annual International Conference on Mobile Computing And Networking*, pages 310–323, 2022.

[43] Don H Johnson. Signal-to-noise ratio. *Scholarpedia*, 1(12):2088, 2006.

[44] Todd B Parrish, Darren R Gitelman, Kevin S LaBar, and M-Marsel Mesulam. Impact of signal-to-noise on functional mri. *Magnetic Resonance in Medicine: An Official Journal of the International Society for Magnetic Resonance in Medicine*, 44(6):925–932, 2000.

[45] Daniel K Sodickson, Mark A Griswold, Peter M Jakob, Robert R Edelman, and Warren J Manning. Signal-to-noise ratio and signal-to-noise efficiency in smash imaging. *Magnetic Resonance in Medicine: An Official Journal of the International Society for Magnetic Resonance in Medicine*, 41(5):1009–1022, 1999.

[46] Feng Zhang, Chenshu Wu, Beibei Wang, and KJ Ray Liu. mmeye: Super-resolution millimeter wave imaging. *IEEE Internet of Things Journal*, 8(8):6995–7008, 2020.

[47] Xiangyu Gao, Sumit Roy, and Guanbin Xing. Mimo-sar: A hier-archical high-resolution imaging algorithm for mmwave fmcw radar in autonomous driving. *IEEE Transactions on Vehicular Technology*, 70(8):7322–7334, 2021.

[48] Mohammad Tayeb Ghasr, Sergey Kharkovsky, Royce Bohnert, Brice Hirst, and Reza Zoughi. 30 ghz linear high-resolution and rapid millimeter wave imaging system for nde. *IEEE transactions on antennas and propagation*, 61(9):4733–4740, 2013.

[49] Paul Suetens. *Fundamentals of medical imaging*. Cambridge university press, 2017.

[50] John L Semmlow. *Biosignal and medical image processing*. CRC press, 2008.

[51] Rebecca Smith-Bindman, Diana L Miglioretti, and Eric B Larson. Rising use of diagnostic medical imaging in a large integrated health system. *Health affairs*, 27(6):1491–1502, 2008.

[52] Molly T Beinfeld and G Scott Gazelle. Diagnostic imaging costs: are they driving up the costs of hospital care? *Radiology*, 235(3):934–939, 2005.

[53] Amani Yousef Owda. Passive millimeter-wave imaging for burns diagnostics under dressing materials. *Sensors*, 22(7):2428, 2022.

[54] Sruthy Skaria, Nermine Hendy, and Akram Al-Hourani. Machine-learning methods for material identification using mmwave radar sensor. *IEEE Sensors Journal*, 23(2):1471–1478, 2022.

[55] Robert Černỳ. Time-domain reflectometry method and its application for measuring moisture content in porous materials: A review. *Measurement*, 42(3):329–336, 2009.

[56] Christof Huebner, Stefan Schlaeger, Rolf Becker, Alexander Scheuermann, Alexander Brandelik, Wolfram Schaedel, and Rainer Schuhmann. Advanced measurement methods in time domain reflectometry for soil moisture determination. In *Electromagnetic Aquametry: Electromagnetic Wave Interaction with Water and Moist Substances*, pages 317–347. Springer, 2005.

[57] E RoTimi Ojo, Paul R Bullock, Jessika L'Heureux, Jarrett Powers, Heather McNairn, and Anna Pacheco. Calibration and evaluation of a frequency domain reflectometry sensor for real-time soil moisture monitoring. *Vadose Zone Journal*, 14(3):vzj2014–08, 2015.

[58] Hailong He, Neil C Turner, Kailin Aogu, Miles Dyck, Hao Feng, Bingcheng Si, Jinxin Wang, and Jialong Lv. Time and frequency domain reflectometry for the measurement of tree stem water content: A review, evaluation, and future perspectives. *Agricultural and Forest Meteorology*, 306:108442, 2021.

[59] Jinghui Xu, Xiaoyi Ma, Sally D Logsdon, and Robert Horton. Short, multineedle frequency domain reflectometry sensor suitable for measuring soil water content. *Soil Science Society of America Journal*, 76(6):1929–1937, 2012.

[60] Nicholas R Harris and Alexander Stonard. A printed capacitance sensor for soil moisture measurement. In *Proceedings*, volume 2, page 705. MDPI, 2018.

[61] Oleksandr Zabolotnyi and Mikola Koshevoi. An effective method of bulk materials moisture measurement using capacitive sensors. *Journal of Stored Products Research*, 89:101733, 2020.

[62] Edwin T Engman and Narinder Chauhan. Status of microwave soil moisture measurements with remote sensing. *Remote Sensing of Environment*, 51(1):189–198, 1995.

[63] Johanna Peters, Wolfgang Taute, Kathrin Bartscher, Claas Döscher, Michael Höft, Reinhard Knöchel, and Jörg Breitkreutz. Design, development and method validation of a novel multi-resonance microwave sensor for moisture measurement. *Analytica chimica acta*, 961:119–127, 2017.

[64] Rasool Keshavarz, Justin Lipman, Dominique MM-P Schreurs, and Negin Shariati. Highly sensitive differential microwave sensor for soil moisture measurement. *IEEE Sensors Journal*, 21(24):27458–27464, 2021.

[65] Usman Mahmood Khan and Muhammad Shahzad. Estimating soil moisture using rf signals. In *Proceedings of the 28th Annual International Conference on Mobile Computing and Networking*, pages 242–254, 2022.

[66] Yuda Feng, Yaxiong Xie, Deepak Ganesan, and Jie Xiong. Lte-based low-cost and low-power soil moisture sensing. In *Proceedings of the 20th ACM Conference on Embedded Networked Sensor Systems*, pages 421–434, 2022.

[67] Jian Ding and Ranveer Chandra. Towards low cost soil sensing using wi-fi. In *The 25th annual international conference on mobile computing and networking*, pages 1–16, 2019.

[68] Wenyao Chen, Yimeng Feng, Mark Cardamis, Cheng Jiang, Wei Song, Oula Ghannoum, and Wen Hu. Soil moisture sensing with mmwave radar. In *Proceedings of the 6th ACM Workshop on Millimeter-Wave and Terahertz Networks and Sensing Systems*, pages 19–24, 2022.

[69] Colleen Josephson, Manikanta Kotaru, Keith Winstein, Sachin Katti, and Ranveer Chandra. Low-cost in-ground soil moisture sensing with radar backscatter tags. In *ACM SIGCAS conference on computing and sustainable societies*, pages 299–311, 2021.

[70] Zhe Yin, Tingwu Lei, Qinghong Yan, Zhanpeng Chen, and Yuequn Dong. A near-infrared reflectance sensor for soil surface moisture measurement. *Computers and electronics in agriculture*, 99:101–107, 2013.

[71] DC Slaughter, MG Pelletier, and SK Upadhyaya. Sensing soil moisture using nir spectroscopy. *Applied engineering in agriculture*, 17(2):241, 2001.

[72] Peter Daugbjerg Jensen, Hans Hartmann, Thorsten Böhm, Michael Temmerman, Fabienne Rabier, and Merete Morsing. Moisture content determination in solid biofuels by dielectric and nir reflection methods. *Biomass and bioenergy*, 30(11):935–943, 2006.

[73] Qijia Guo, Zhongmin Wang, Tianying Chang, and Hong-Liang Cui. Millimeter-wave 3-d imaging testbed with mimo array. *IEEE Transactions on Microwave Theory and Techniques*, 68(3):1164–1174, 2019.

[74] RZ Syeda, TG Savelyev, MC Van Beurden, and AB Smolders. Sparse mimo array for improved 3d mm-wave imaging radar. In *2020 17th European Radar Conference (EuRAD)*, pages 342–345. IEEE, 2021.

[75] Gerard Rankin, Andrew Tirkel, and Anatolii Leukhin. Millimeter wave array for uav imaging mimo radar. In *2015 16th International Radar Symposium (IRS)*, pages 499–504. IEEE, 2015.

[76] Yan Zhao, Weikang Si, Bingxin Han, Zihan Yang, Anyong Hu, and Jungang Miao. A novel near field image reconstruction method based on beamforming technique for real-time passive millimeter wave imaging. *IEEE Access*, 10:32879–32888, 2022.

[77] Andreas Schiessl, Sherif Sayed Ahmed, Andreas Genghammer, and Lorenz-Peter Schmidt. A technology demonstrator for a 0.5 mx 0.5 m fully electronic digital beamforming mm-wave imaging system. In *Proceedings of the 5th European Conference on Antennas and Propagation (EUCAP)*, pages 2606–2609. IEEE, 2011.

[78] Nafiseh Mohammadian, Orges Furxhi, Robert Short, and Ronald Driggers. Sar millimeter wave imaging systems. In *Passive and Active Millimeter-Wave Imaging XXII*, volume 10994, pages 86–98. SPIE, 2019.

[79] Maximilian Steiner, Timo Grebner, and Christian Waldschmidt. Millimeter-wave sar-imaging with radar networks based on radar self-localization. *IEEE Transactions on Microwave Theory and Techniques*, 68(11):4652–4661, 2020.

[80] Hem Regmi, Moh Sabbir Saadat, Sanjib Sur, and Srihari Nelakuditi. Squigglemilli: Approximating sar imaging on mobile millimeter-wave devices. *Proceedings of the ACM on Interactive, Mobile, Wearable and Ubiquitous Technologies*, 5(3):1–26, 2021.

[81] Moh Sabbir Saadat, Sanjib Sur, Srihari Nelakuditi, and Parmesh Ramanathan. Millicam: Hand-held millimeter-wave imaging. In *2020 29th International Conference on Computer Communications and Networks (ICCCN)*, pages 1–9. IEEE, 2020.